Thermogravimetric and Microstructural Analysis of the Oxidation of Iron Powders

Quentin Fradet*[a], Syafinah Fong[a], Michalina Kurnatowska[a], Antonio Soria-Verdugo[b], Laurine Choisez[c], Uwe Riedel[a]

[a] German Aerospace Center (DLR), Institute of Low-Carbon Industrial Processes, Walther-Pauer-Straße 5, Cottbus 03046, Germany (quentin.fradet@dlr.de).

[b] Department of Thermal Engineering and Fluid Mechanics, University Carlos III of Madrid, Butarque 15, 28911 Madrid, Spain (asoria@ing.uc3m.es).

[c] UCLouvain, Institute of Mechanics, Materials and Civil Engineering, IMAP, Place Sainte 2, B-1348 Louvain-la-Neuve, Belgium (laurine.choisez@uclouvain.be).

***** Correspondence should be addressed to Quentin Fradet (phone number: +49 355 355 645 14)

Abstract

Metal fuels, particularly iron, hold great promise as a sustainable source for decarbonating heat or electricity supply. However, a comprehensive understanding of the physics governing the combustion of iron dust flames is currently lacking. In this study, we present a thorough kinetic investigation of the oxidation of iron micrometer particles. Thermogravimetric analysis experiments were conducted under isothermal conditions and with varying uniform heating rates, with air, and with pure oxygen, as well as with various powders. Our results indicate that the oxidation of iron particles can achieve completion at relatively low temperatures, even before the appearance of wüstite. Microstructural analysis revealed an oxidation process under 570 °C dominated by the growth of a duplex magnetite layer, surrounded by a network of hematite ridges. In later stages of oxidation, a continuous surface might form, drastically hindering the contact between the iron material and the oxidizing agent. A preliminary kinetic analysis has been conducted using model-free and model-fitting methods. An approximate activation energy of 220 kJ/mol has been derived from the Kissinger-Akahira-Sunose method and it is shown that the truncated Sestak and Berggren model could fairly reproduce isothermal and dynamic thermogravimetric analysis experiments.

Keywords. Iron powder; Metal fuel; Thermogravimetric analysis; Oxidation kinetics.

1. Introduction

Metals and their oxides can be used in oxidation-reduction cycles for large-scale power generation, resulting in CO_2-free energy conversion [1] [2]. Recent research efforts have been in particular put on iron [3], as its dry oxidation comes with limited nanoparticle formation in contrast to other metal fuels. Further advantages of iron include its large abundance, relatively low-costs and safety hazard. Iron-based combustion technology is quickly developing, currently reaching the MW level [4], but the room for improvements is important, including minimizing material losses, maximizing fuel conversion, avoiding slag accumulation, or optimizing the cyclability of the process.

Combustion modeling, for example with computational fluid dynamics (CFD) simulations, has become an essential tool for optimizing burner design and performance. However, this requires an accurate model for the oxidation kinetics, which is currently lacking. After a certain run-away temperature [5], the process is mostly limited by oxygen diffusion, but a crucial part of the process is governed by slower kinetic phenomenon. Mich et al. [6] tested three different oxidation models and showed that they led to very different reaction front speeds, which greatly influence the overall combustion behavior. Studies tackling the oxidation kinetics of iron particles are scarce. Therefore, recent works on the combustion of iron dust rely on well-established kinetic data derived from oxidation experiments on iron strips. But to which extent those are transposable for micron-sized particles is an open question. The main objective of the present study is to provide a first understanding of the oxidation of iron and derive first kinetic data. It should shed light on the species in presence, on the rate limiting steps, and on the oxide growth mechanism. A particular focus is put on the “low” temperature oxidation, meaning up to 570 °C. This temperature is a threshold for the appearance of wüstite, and thus, the oxidation mechanism differs quite radically.

This paper opens with a dedicated section on the literature on iron oxidation, because metal oxidation in general is an already thouroughly studied research topic. And while peculiarities are associated to the oxidation of powders, the governing physics should essentially be common. Therefore, this section first reviews the theory of metal oxidation, then the current state of understanding of the oxidation of iron strips is presented, and finally the few studies on iron particle oxidation are examined. The following section briefly presents the material, experimental methods, and modelling approaches utilized in this study. Briefly summarized, the kinetic study is based on a comprehensive

thermogravimetric analysis (TGA) test campaign consisting of approximately 100 individual experiments on two iron samples of about 8 μm diameter, particle characterization with scanning electron microscopy (SEM) and X-ray diffraction (XRD) analysis, and standard gas-solid kinetic methods. In the last section, the main results are briefly presented, then these data are interpreted in more detail, including making the link with the product characterization and proposing a mechanism for the oxidation process of micron-sized particles. Some directions for future research are also suggested to close the remaining knowledge gap.

2. Literature review on the oxidation of iron

Oxidation of metals occurs when exposed metallic surfaces come into contact with oxidizing elements, typically oxygen [7]. This process is initiated by the adsorption and chemisorption of oxygen onto the metallic surface. As the coverage progresses, a primary oxide layer forms through nucleation and lateral growth, covering the entire surface [8]. Once established, further growth of the oxide layer can occur if the transport of ions and electrons across the oxide film is possible.

For this transport to happen, points defects within the oxide film are necessary. Those defects are typically vacant lattice sites (for example, a cation vacancy in the cation sub-lattice paired with an anion vacancy in the anion sub-lattice). Ions can jump to surrounding point defect sites, which eventually induces a migration for the metal/oxide interface to the oxide/air interface. Electrons must as well migrate to the oxide/atmosphere interface, where they are involved in oxygen ionization. The electron transport mechanism via vacant sites can be slow because of electrical neutrality, but electron migration can be much faster when ions, generally cations, exhibit variable valences. If electron transport is much faster than cation, this create a negative space charge, which accelerate the migration of cations. The influence of the electric field on the transfer of metal wanes with increasing oxide layer thickness, thus, this mechanism is only valid for thin films. Above a certain transition thickness, whose reference value is 1 μm [9], one speaks of thick film growth. This reference value is only indicative, as it depends from one metal to the other, the conditions of temperature etc. but it should be noticed that it is of comparable size order than the particle diameters under consideration in this study. Under the thin film assumption, many theories have been developed leading to multiple rate laws. For example, Mott's initial work [10] suggests that electron tunneling is rate limiting, following a direct logarithmic relationship, while the Cabrera-Mott theory [11] stipulates that at some later stage, ion migration because rate limiting, inducing an inverse logarithmic law.

In contrast, for thick films where space charges play a negligible role, self-diffusion within the oxide film is the primary growth mechanism. This leads to the most known Wagner's theory of thick film growth [12] [13]. Among the numerous assumptions, which can be reviewed in Atkison et al. 1988 [14], it is assumed that diffusion of charged species is rate limiting. The charged species might as well be metal cations, oxygen anions, electrons, or electron holes, depending on the point defects and electronic structure of the oxide. This diffusion supposes a gradient in the chemical potential across the film acting as a driving force. The flux of charged species is inversely proportional to the film thickness, and therefore, a parabolic growth rate is obtained, which has been in many cases experimentally observed. However, the oxidation rate is usually several orders of magnitude greater than expected by calculation from the diffusion coefficients. Two main reasons are put forward by Atkinson et al. 1988 [14], the presence of short circuit diffusion pathways through the film and point defect concentrations from the presence of impurities. Short circuits might stem from dislocations, grain boundaries, or interconnected porosity within the oxide.

As presently seen, there is a common knowledge base on the oxidation of metals. However, the uniqueness of the individual metals and their oxides makes it necessary to restrain the scope to the iron-oxide system. Iron is arguably the most studied metal when it comes to the oxidation process, spanning from theoretical studies, as iron is the most common metal, to more practical studies on corrosion, as its usage as steel is widespread in all industry applications. The iron-oxide system counts three distinct oxides, with simplified stoichiometric formulas FeO (wüstite), Fe_3O_4 (magnetite), and Fe_2O_3 (hematite). In reality, small deviation from stoichiometry is common, in particular wüstite is metal deficient and presents the peculiarity to be unstable below about 570 °C. Wüstite cation's sub-lattice is composed of ferrous ions Fe^{2+} and hematite of ferric ions Fe^{3+}. Magnetite is composed of both ions in the ratio $Fe^{2+}: Fe^{3+} = 1:2$. A general observation made among metals featuring several oxide layers is that the highest oxygen-rich oxide is found in contact with the atmosphere and the lowest in contact with the metal. For iron, this would mean up to three oxide layers $FeO - Fe_3O_4 - Fe_2O_3$ (in order starting from the metal) with oxygen accounting for 22.3, 27.6, and $30.1\%_{wt}$ in their stoichiometric forms, respectively. This has been indeed reported for temperature above 570 °C [15]. The scales (usual name given to the oxide film of important size) is primarily made of wüstite, then magnetite, and a very thin layer of hematite, sometimes even ignored. The exact ratio between the oxides depends on the temperature, oxygen partial pressure, and characteristics of the iron specimen, but nearly constant values of 95:4:1% are reported above 700 °C [15] [16] [17] [18].

At lower temperatures (between 225 to 570 °C, that mean the particular focus of this study), only magnetite and hematite form. Around 225 °C, a majority of hematite is observed, but the proportion of hematite decreases with increasing temperature [19]. At 500 °C, up to ten times more magnetite than hematite has been reported [20]. At 550 °C, the thickness ratio of hematite to magnetite approaches a value of 5% [21]. But the scale structures forming under this temperature range and the associated kinetic rates are significantly influenced by the preparation of the samples [22] [23]. Generally, cold-worked samples exhibit much faster oxidation, especially in the initial stages, compared to annealed samples. This can be attributed to the gradual reduction in contact between the scale and the iron substrate. In areas where the scale remains in contact, it appears relatively thick, whereas in locations where the scale-iron contact is lost, it appears very thin. In extreme cases, certain regions, where the scale-iron contact was entirely lost, showed a unique hematite layer. Some authors also found a duplex magnetite layer [21] [24] [25]. A duplex layer designates two structurally distinct layers of a same oxide. Atkinson et al. [9] thoroughly described their structure and possible formation mechanism. The outer layer has a columnar structure formed by the outward diffusion of metal ions while the inner layer is more equi-axed and grows by the inward short-circuit transport of oxygen.

As magnetite might be the prevalent oxide in the condition of the present study, a particular attention can be put on the rate-controlling transport mechanisms within magnetite films. In the early study of Davies et al. [15], the authors estimated that 80% of the oxide growth was due to anion diffusion and 20% from ferrous ion diffusion. But a footnote in paper from Himmel et al. [26] indicates that there might have been an interpretation error. Bruce [7] compared the self-diffusion coefficient of iron in magnetite and that of oxygen in magnetite and found that the latter is 10^4 lower at 500 °C. For the author to conclude that the oxygen diffusion plays a minor role in the growth of magnetite. Limitations to this analysis is that it does not account for short circuit pathways, and the diffusion coefficient for iron was extrapolated from the temperature range 800-1000 °C to 500 °C. But, this suggestion is further supported by the research of Bertrand et al. [25], who performed oxidation tests on pure iron sheets at low temperatures (260–400 °C). They determined that the rate-controlling step in oxidation kinetics is cation diffusion in the outer magnetite layer of the duplex structure. The thickness of this layer controls the amount of inward diffusion of oxygen through its short circuits and then controls the growth kinetics of the internal magnetite layer. According to their mechanism, the growth rates of the various oxide layers depend on each other and this explains why the proportion of the ratio of oxide layers thicknesses remains constant. At an early stage, before nucleation of a hematite layer, magnetite might form directly at the magnetite/air interface [27]. This growth subsequently slows down when the hematite layer has nucleated.

Thereafter, the oxygen partial pressure for the magnetite outward growth corresponds to the dissociation pressure of hematite. Magnetite forms by the reduction of the overlying hematite layer:

$$Fe^{n+} + n\,e^{-} + 4\,Fe_2O_3 \rightarrow 3\,Fe_3O_4. \quad (X)$$

As previously mentioned, the growth rates are greater than calculated from Wagner's theory. Deviations are particularly important below 570 °C. Furthermore, the values are scattered. However, the proposed activation energies, that means the dependency of these growth values with the temperature, are in a rather narrow range: 105 kJ/mol [28] for a temperature range of oxidation of 250-350 °C, 149 kJ/mol [29] for the range 250-375 °C, 134 kJ/mol [30] for the range 200-400 °C, 151 kJ/mol [25] for the range 260-500 °C, 130 kJ/mol [31] for the range 450-550 °C. These values are considerably smaller than the self-diffusion coefficient of iron in magnetite (230 kJ/mol) [26]. All above elements suggest the strong contribution of short circuits in the growth mechanism.

The formation of hematite is often overlooked, especially because of the negligible formed quantity at high temperatures. However, its absence or presence greatly influence the overall growth rate, and thus understanding its formation mechanism is also of importance. One condition for its presence might be that the magnetite grows to a certain thickness, so that this layer growth rate falls behind the nucleation of hematite [19]. The nucleation of hematite seems to increase with the oxygen partial pressure [27]. As the growth of hematite is promoted, the growth of magnetite decreases, and thus the overall growth is deteriorated. The growth of hematite can as well be achieved by the migration of iron cation to the hematite/air interface than by the inward migration of anions to the magnetite/hematite interface. The report growth value are here also several times larger than both the self-diffusion coefficients of oxygen and of iron in hematite [26] [32]. This external layer of hematite is described as being made of equiaxed grains [25], only a few grains thick [21]. Externally, a network of ridges forms a cellular or honeycomb pattern [16] [20]. Many studies also report the presence of whiskers/blades/nanowires growing out of the surface oxide. Those consists of single hematite crystals [33] and could be found under various conditions of oxidizing environment with temperatures comprised between 400 to 800 °C [34]. These blades might grow from surface diffusion of iron cations from the underlying magnetite through the tunnels to the blade tips [35] [36]. Interestingly, such nanowires have been reported on iron microparticles oxidized in ambient air at 255 °C [37], here also purely composed of hematite.

To conclude this literature review, the focus will now be put on the so-far published works on the oxidation of iron particles. The publication of Lysenko et al. [38] investigated the kinetics of iron powder oxidation using thermogravimetric analysis (TGA), however on particles in the nanometer range. Three

samples with mean particle sizes ranging from 90 to 350 nm were studied. The samples were always oxidized below 567 °C. The composition analysis of the products revealed the presence of magnetite and hematite. The authors concluded that a three-step process was taking place, with competing oxidation from Fe to hematite or magnetite, and the ultimate oxidation from magnetite to hematite. This was their explanation for the apparent two-stage oxidation under linear increase of the temperature. But a publication also using nanoparticles supplied by a Russian commercial company and made by the electric explosion of wire, revealed a bimodal distribution of the powders [39], which might explain the TGA profiles. Indeed, it is quite apparent that the particle size is a primary influence parameter of the oxidation rate. Mandilas et al. [40] performed TGA on nanoparticles, with mean sizes between 25 and 85 nm and one TGA experiment with a reference sample between 6 and 10 micrometers. The TGA curve under linear temperature increase of the sample with micrometer particles is shifted by about 150 °C compared to the samples with nanometer particles and a plateau is reached at about 567 °C. They studied the effect of oxygen concentration and found that increasing the oxygen content from 2% to 21% accelerated oxidation, but no notable differences were identified between synthetic air and pure oxygen environments. In another paper, Lysenko et al. [41] showed that the presence of wüstite in the original powder shifts the reaction to higher temperatures. More recently, Kuhn et al. [42] investigated the oxidation behavior or iron particles in the micrometer range based on thermogravimetric analysis. They showed the dependency of the rate of oxidation with both the particle size and oxidation temperature. The authors further demonstrated that the cyclization of iron particles enhances reactivity, which they attributed to increased porosity of the particles.

3. Materials and Methods

3.1. Thermogravimetric experiments

Two iron powder samples have served for the purpose of this article. The first sample used in this experiment was a commercial iron powder obtained from Carl Roth GmbH, Karlsruhe, Germany (article N° 3718.1). It has a mean diameter of 8 micrometers and a purity level exceeding 99.5% [43]. The second sample was also carbonyl iron powder, but from Sigma-Aldrich (product number 12310) a purity level above 99%. Though it can be found in the literature that this powder is composed of much larger particles with a mean diameter of 120 µm [44], our analysis revealed a particle size distribution very close to the powder from Carl Roth. Details on the conducted analysis and on the results will be given in sections 3.2

and 4.1. In the following, powders A and B designate the samples from Carl Roth and Sigma-Aldrich, respectively.

A comprehensive TGA test campaign on the oxidation behavior of the previously mentioned powders has been conducted. The detailed list of experiments is given in Table 1. This list also gives the corresponding figures to each experimental set, that they are to be found in the remainder of the paper or in the supplementary materials. Two different TGA instruments - a Linseis STA PT 1600 apparatus and a thermogravimetric analyzer TGA Q500 from TA Instruments - were used and most of the tests have been conducted multiple times to ensure their reproducibility. Flat platinum sample pans were used for both non-isothermal and isothermal tests, and the sample initially of about 28 mg was homogenously distributed on the pan to improve the contact of the sample with oxygen. Non-isothermal and isothermal experimental measurements were performed. For non-isothermal oxidation tests, a linear increase in temperature from ambient to 900 ºC was used, at constant heating rates of 1, 2, 5, 10, and 15 °C/min. Isothermal oxidation was also studied, increasing the temperature from ambient to the oxidation temperature, while supplying the furnace with a flow rate of nitrogen to guarantee inert conditions for the sample until the desired temperature was reached. Then, the flow was suddenly changed to supply the oxidizing gas, either air or pure oxygen, at a constant temperature for at least 60 min. The oxidation temperatures tested for the isothermal experiments ranges from 300 to 700 °C, with a particular focus in the range 400 to 570 °C. The tests were performed by supplying a constant flow rate (of 60 to 100 ml/min in the regular cases) of oxidizing gas, namely air or oxygen, to the furnace. Tests with variation of the gas flow rate and initial solid weight were also conducted to study the effect of the two operating parameters.

Table 1. Experiments conducted in this study and the corresponding operating conditions.

Denomination of experiment groups	TGA device	Sample and mass	Gas conditions	Temperature conditions	Associated figure(s)
Q500_PB_Air_Iso	TA Instruments Q500	Powder A ~28 mg	Air 60 mL/min	Isothermal 300, 350, 400, 450, 500, 550 °C	Figure 2 Figure 3 Figure S1 Figure S2
PT1600_PA_Air_Iso	Linseis TGA PT 1600	Powder A ~28 mg	Air 100 mL/min	Isothermal 300, 350, 400, 450, 500, 550 °C	Figure S2
Q500_PB_Air_Iso	TA Instruments Q500	Powder B ~28 mg	Air 60 mL/min	Isothermal 300, 350, 400, 450, 500, 550 °C	Figure S2
PT1600_PB_Air_Iso	Linseis TGA PT 1600	Powder B ~28 mg	Air 100 mL/min	Isothermal 300, 350, 400, 450, 500, 550 °C	Figure S2
PT1600_PB_Air_Flow	Linseis TGA PT 1600	Powder B ~28 mg	Air 20, 200 mL/min	Isothermal 400 °C	Figure 4
Q500_PA_Air_Iso_HighT	TA Instruments Q500	Powder A ~28 mg	Air 60 mL/min	Isothermal 570, 600, 650, 700 °C	Figure 5

PT1600_PAB_Air_Step	Linseis TGA PT 1600	Powder A & B ~28 mg	Air 100 mL/min	Stepwise Isothermal 300-400-500 °C	Figure 6
Q500_PB_O2_Iso	TA Instruments Q500	Powder B ~28 mg	O_2 60 mL/min	Isothermal 300, 350, 400, 450, 500, 550 °C	Figure 7 Figure S3
Q500_PB_Air_Lin	TA Instruments Q500	Powder B ~28 mg	Air 60 mL/min	Linear increase 1, 2, 5, 10, 15 °C/min	**Erreur ! Source du renvoi introuvable.** Figure 9
PT1600_PB_Air_Lin	Linseis TGA PT 1600	Powder B ~28 mg	Air 100 mL/min	Linear increase 1, 2, 5, 10, 15 °C/min	Figure S4
PT1600_PA_Air_Lin	Linseis TGA PT 1600	Powder A ~28 mg	Air 100 mL/min	Linear increase 1, 2, 5, 10, 15 °C/min	Figure S4
Q500_PB_O2_Lin	TA Instruments Q500	Powder B ~28 mg	O_2 60 mL/min	Isothermal: 300, 350, 400, 450, 500, 550 °C	Figure 11
PT1600_PA_Air_Iso_HighM	Linseis TGA PT 1600	Powder A ~300 mg	Air 100 mL/min	Isothermal 400 °C	Figure S5 (No data)
PT1600_PAB_Air_Lin_HighM	Linseis TGA PT 1600	Powder A & B ~300 mg	Air 100 mL/min	Linear increase 5 °C/min	Figure S5

3.2. Microstructure characterization

To gain further understanding of the oxidation process, structure characterization techniques have been applied to the raw materials and to the oxidation products. These techniques are respectively scanning electron microscopy and X-ray diffraction. The products that were tested originated from the oxidation at 5 °C/min, either up to a point corresponding to 50% of oxidation or up to temperatures of 700 or 900 °C, as well as after two hours of oxidation at 400 °C. In order to obtain accurate XRD analysis, the necessary product weights were collected by running multiple oxidation experiments with an initial sample mass of 300 mg. The phases were identified and their average fractions analyzed using a diffractometer D8 Advance A25-X1. The diffractometer was operated with a cobalt target at 35 kV and 40 mA. The phase distribution was quantified by Rietveld refinement using the software Bruker TOPAS Version 5.0. The oxidized products formed single-block sinters. The SEM images, probed by the apparatus Zeiss Sigma, were taken of the sinter face that was in contact with the crucible.

3.3. Kinetic modeling approaches

The thermal analysis experiments of this paper are reported as the sample mass evolution, more precisely as the ratio of the sample weight at a certain time, $m(t)$, to the initial sample weight, m_0. It is common in gas-solid kinetic methods to rather use the conversion degree, or in the present case, the extent of oxidation α. By assuming the sample to be composed of 100% iron, and taking hematite as the final stage of oxidation, it is defined as:

$$\alpha = \frac{m(t)-m_0}{m_\infty - m_0}, \quad \text{(X)}$$

where:

$$m_\infty = \frac{M_{Fe_2O_3}}{2\,M_{Fe}} m_0 \approx 0.14297 m_0. \quad \text{(X)}$$

In the previous equation, the m_∞ is theoretical mass after complete oxidation, and M the molar weight.

In the present kinetic analysis, it is assumed, as commonly done, that the conversion rate can be expressed according to the general formulation:

$$\frac{\mathrm{d}\alpha}{\mathrm{d}t} = f(\alpha)k(T), \quad \text{(X)}$$

where $f(\alpha)$ is the reaction model and is $k(T)$ is the rate constant, which represents the dependence of the process rate on temperature, typically expressed by the Arrhenius equation. Among the classical gas-solid kinetic methods, one can make the distinction between two groups of methods, the isoconversional methods and the model-fitting methods [45] [46].

In the first group of methods, no determination of the reaction model is needed, hence they are commonly named model-free methods. One such method is the Kissinger method (refs), which allows the determination of the activation energy from a series of experiments with varying linear heating rates β. The method relies on the fact that at there is a certain temperature T_{max}, where the reaction rate is maximum, and thus the second derivative of the conversion degree with respect to time is zero. The following equation can be derived:

$$\ln\left(\frac{\beta}{T_{max}^2}\right) = \ln\left(-\frac{AR}{E_a}\frac{\mathrm{d}f}{\mathrm{d}\alpha}\right) - \frac{E_a}{RT_{max}}. \quad \text{(X)}$$

Plotting the left-hand side of the previous equations against a $1/T_{max}$ from experiments with varying linear heating rates should therefore whose slope yields the activation energy. Another model-free method used in this paper is the Kissinger–Akahira–Sunose (KAS) method, which also serve to derive the activation energy from TGA experiments with constant heating rates. The final equation is similar to the one of the Kissinger method

$$\ln\left(\frac{\beta}{T_\alpha^2}\right) = \mathrm{Const} - \frac{E_a}{RT_\alpha}, \quad \text{(X)}$$

but with RT_α, that means the temperature at which a certain conversion degree is reach. Similarly plotting the left-hand side for a series of experiments versus $1/T_\alpha$ gives the activation. Where the Kissinger

yielded a unique activation energy value, the KAS method can be applied at different values of α, or even continuously from $\alpha = 0$ to α_∞.

The second group of methods, i.e. the model-fitting methods, requires an assumption of the mathematical expression for the reaction model $f(\alpha)$. Denominations and code names proposed by the ICTAC kinetics committee [47] are used in the result section. Many information can be gathered from a simple reading of the TGA curve profiles under isothermal conditions. Whether they show a decelerating, sigmoidal, or accelerating profile can guide for the choice of possible reaction models. Confronting the kinetic data to microstructural analysis can further comfort the model choice [48]. Further testing of different reaction models can be done for isothermal runs by rearranging and integrating equation X:

$$\frac{\mathrm{d}\alpha}{f(\alpha)} = k(T)\mathrm{d}t, \quad \text{(X)}$$

$$\int_0^\alpha \frac{\mathrm{d}\alpha}{f(\alpha)} = g(\alpha) = k(T)t. \quad \text{(X)}$$

Thus, plotting the integral form, $g(\alpha)$, versus the time for a single experiment should yield a straight line if the right reaction model is picked.

The methods described previously, both isoconversional and model-fitting, are valid under certain assumptions. Notably, multiple step kinetics can bring these methods to their limitations. The result section will analyze, which methods are most-suited in the case of the oxidation process, and what other approaches could be followed next.

4. Results and Discussion

4.1. Initial powders

SEM images of the raw powders A and B can be found in Figure 1. No strong difference between the two powders are noticeable. They are composed of small near-spherical particles of about ~1-5 µm in diameter and are generally agglomerated with other particles. Some larger blocks of 50-100 µm could also be found in both samples. In Figure SX of the supplementary materials, indicative particle size distributions can be found. The distributions reveal the large similarity between the two powders, with mean particle sizes of X and X for powder A and B, respectively. The XRD analysis, also given in the supplementary materials, reveal the high purity of the iron particles.

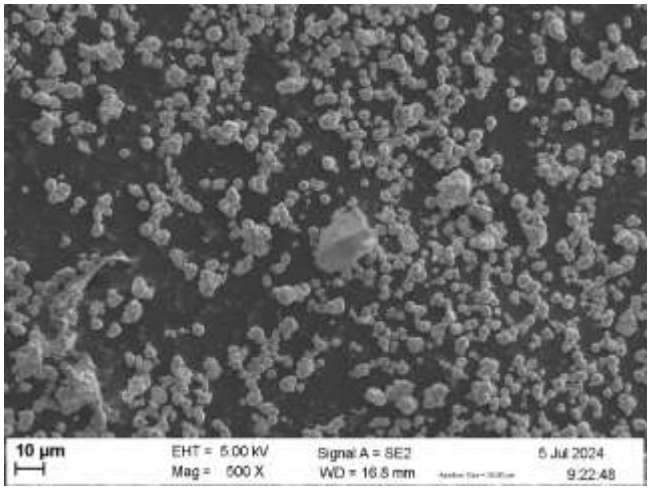

a.

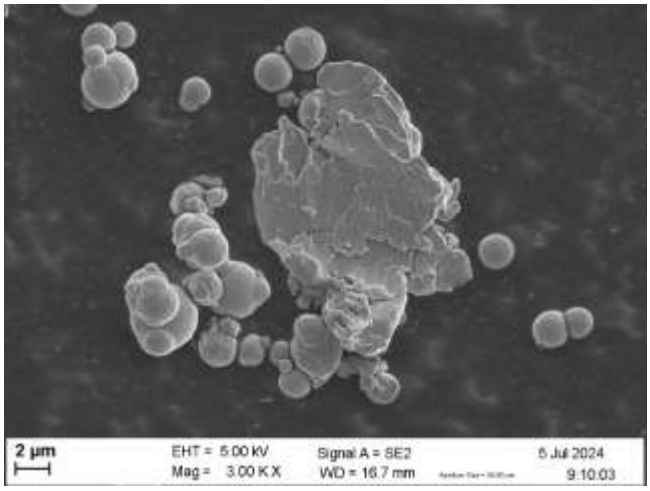

b.

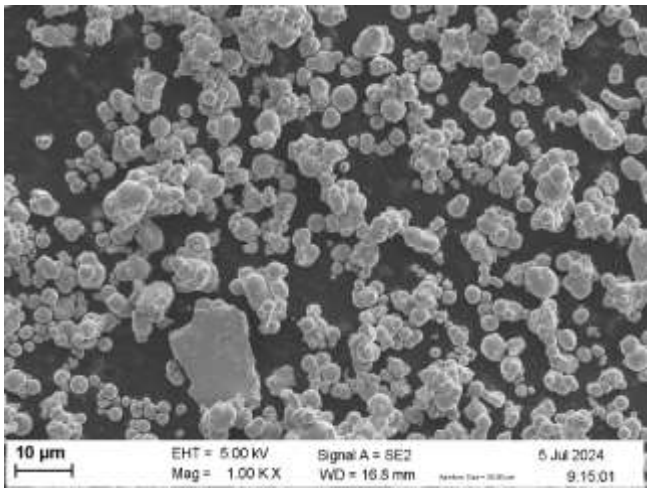

c.

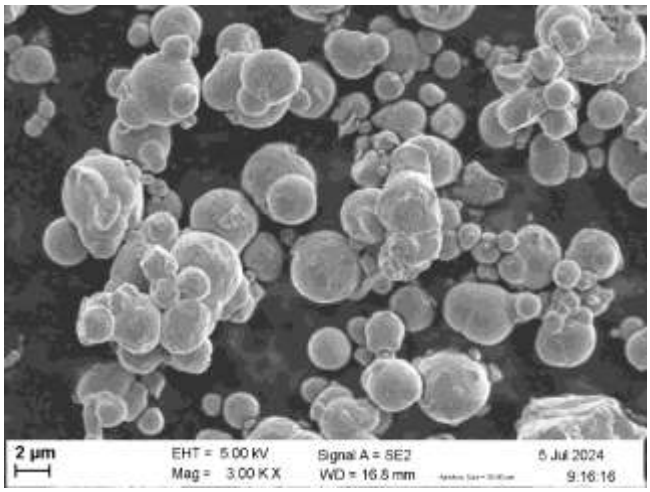

d.

Figure 1. SEM images of the raw powders A and B

4.2. Oxidation under isothermal conditions

The major results of the thermogravimetric measurements conducted under isothermal conditions are presented in Figure 2. In the interest of clarity and visual representation, the figures presented here and in the following sections show a smaller number of experimental points than were actually recorded. A close-up on the 300 first seconds can also be found in the supplementary materials. All curves exhibit a similar shape, with an initial stage – almost linear – of rapid oxidation followed by a second stage with a markedly slower oxidation rate. The slope during the initial stage is nearly identical for all experiments (about 8 percent of weight gain per minute), though a slight increase with temperature can be discerned. But the extent of the initial stage increases with the temperature, resulting in a corresponding increase in the oxidation degree over the course of one hour. Specifically, the mass gain at 300 °C after one hour is

only 3.3%, corresponding to an oxidation degree of 7.7% relative to the maximum theoretical value, while at 550 °C, the mass change is 37.5%, or, in other terms, the material has oxidized to 87.2%.

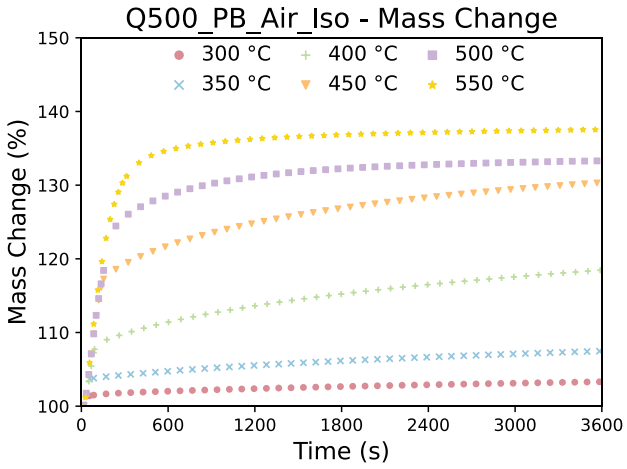

Figure 2. Thermogravimetric analysis of powder B under isothermal conditions

The reproducibility of the experimental results, as well as further data with the second TGA apparatus and the other powder, are given in Figure S2. The results are very consistent over several experiment replications for set temperatures from 300 to 500 °C, and that for both oxidation stages. The experiments run at 550 °C show more variability. In numerous cases, the first stage stops promptly before the 450 and 500°C instances, and the second stage is marked with no significant increase in oxidation. These elements suggest that at elevated temperatures, the oxidation is more sensitive to the experimental preparation, such as the even distribution of iron material on the crucible. The results obtained with either apparatus are comparable, and the minor discrepancies can be attributed to the specific flow patterns within the furnace or the shape and material of the crucibles employed. Furthermore, the oxidation profiles of powders A and B are similar. Powder A may exhibit a slightly faster oxidation rate. However, the differences are within the range of experimental uncertainties.

The variation in temperature over the course of each individual experiment has been recorded. The data are presented in Figure 3 for the oxidation of powder B. It can be observed that a temperature increase occurs when the gas is switched between the inert and the air atmosphere. This can be attributed to the exothermic nature of the oxidation reactions between iron and air. The temperatures subsequently stabilize to the set temperatures more or less rapidly. The duration of this stabilization period manifestly depends on the duration of the rapid oxidation stage. The amplitude of this temperature offset differs between experiments, and although it represents a mere few degrees, the measurements are acquired via

a thermocouple for the gas phase. It can be assumed that the temperature increase for the iron particles is significantly higher.

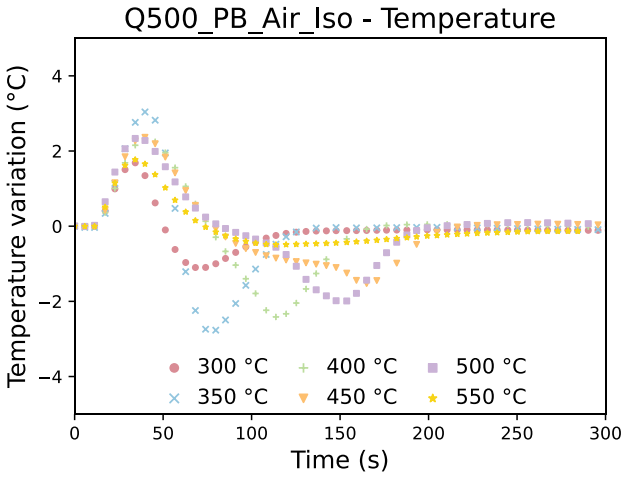

Figure 3. Deviation to the set temperatures for the thermogravimetric analysis of powder B under isothermal conditions

The effect of air flow rate is shown in Figure 4. Three different flow rates, with values of 20, 100, and 200 mL/min, have been employed at the same temperature of 400 °C. The slope of each of the three curves is notably different, accounting for, in order, 2.3, 5.5, and 9.1 percentage points of mass gain per minute. The extent of oxidation is greater for the highest flow rate case, but very similar for the two others. The slow oxidation stage proceeds at a similar rate for all experiments.

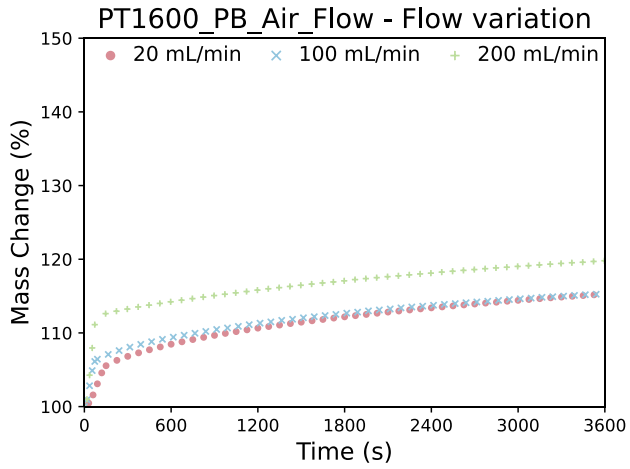

Figure 4. Variation of the gas flow rate at 400 °C

Some results at temperatures 570 °C and higher are given in Figure 5. The curve shapes are rather similar to those observed at lower temperatures, with two distinct stages, but the extent of oxidation does not appear to increase monotonically with increasing temperature. As noted previously for the 550 °C case, the extent of oxidation may be susceptible to experimental preparation. But the global trend given by Figure 5 might be that the extent of oxidation slightly decreases from 570 °C to 700 °C. The main gain after one hour is around 26 to 36%. For comparison, the mass gain associated with the oxidation of iron to stoichiometric wüstite would be 29%. One assumption can therefore be that the oxidation proceeds primarily to wüstite rather than magnetite or hematite, but it could also be related to strong sintering preventing further oxidation of the sample.

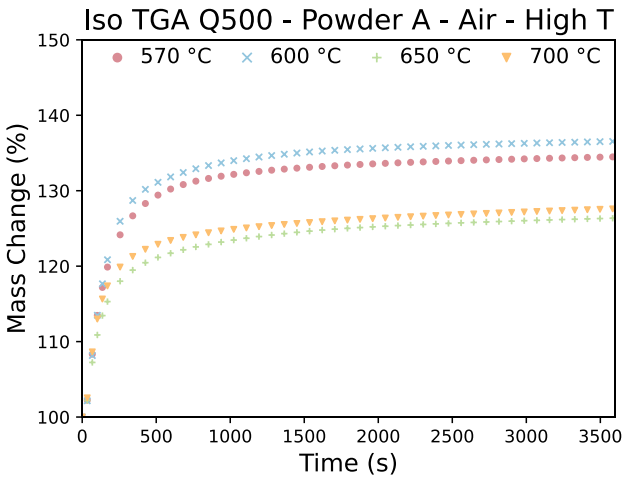

Figure 5. Thermogravimetric analysis of powder A under isothermal conditions at high temperatures

Figure 6 depicts the thermogravimetric results obtained by incrementally elevating the temperature (300, then 400, then 500 °C) over the course of one hour at each step with one-hour operation at each temperature. The figure shows that the process, albeit entering a slow oxidation stage, can be re-accelerated by increasing the temperature. Once more, both powders exhibit comparable oxidation behaviors. However, following each temperature increment, two distinctive stages are not identified; rather, a single parabolic decelerating profile is observed. Additionally, it is notable that the extent of oxidation at the end of each temperature interval is slightly higher compared to the regular isothermal experiments (see, for example, Figure 2).

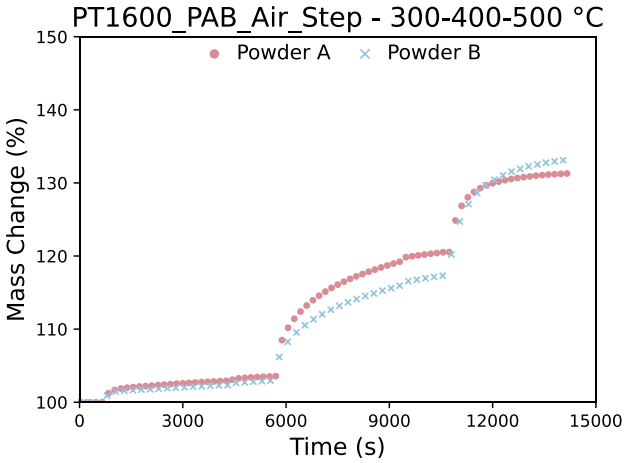

Figure 6. Thermogravimetric analysis of powder A under isothermal conditions at high temperatures

The effect of utilizing pure oxygen on the oxidation process under isothermal conditions can be appreciated in Figure 7. Here also, a close-up on the first 300 seconds and the temperature profiles can be found in the supplementary materials. The two stages are more pronounced than with air. Apart from the 300 °C case, which is an outlier, the oxidation initially follows a linear profile, with a slope of approximately 21%$_{wt}$ gain per minute, which is approximately three times faster than with air, while the oxygen concentration is approximately five folds higher. Conversely, the second stage is comparatively slow, approaching near-zero mass increase rates in many cases. With regard to the temperature evolution, it can be observed that the offset is significantly greater than that observed when using air, reaching a value of approximately 20 °C for the 350 °C case.

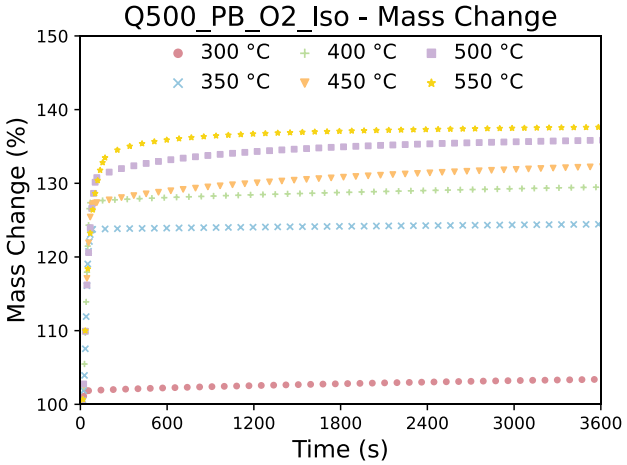

Figure 7. Thermogravimetric analysis of powder A under isothermal conditions at high temperatures

4.3. Oxidation under a linear increase of the temperature

The mass evolution of the TGA experiments with air under linear conditions using the Q500 TGA apparatus are shown in Figure 8. The mass change for the experiments at 1, 2, and 5 °C/min reached 142.7 to 143.0%, which corresponds precisely to the theoretical value of the complete oxidation from iron to hematite. The experiments at 10 and 15 °C/min show on the other hand an advanced but incomplete oxidation, 141.1 and 141.3% at 900 °C, respectively. The oxidation starts in all experiments at around 200 °C. No distinct successive step can be observed, the rate of oxidation gradually increases up to about 500 °C and 50% of oxidation, then gradually decreases.

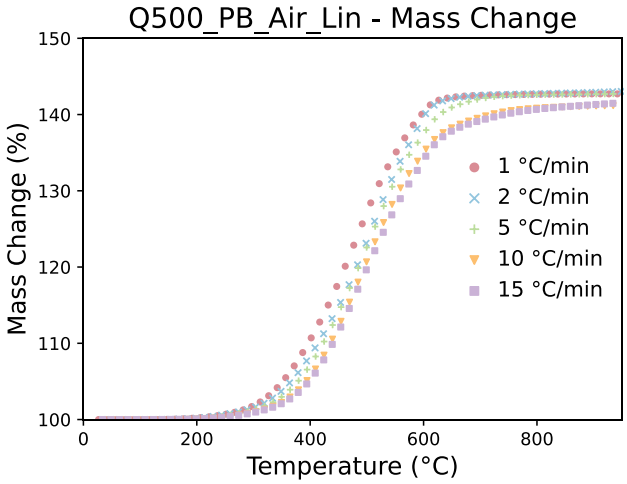

Figure 8. Thermogravimetric analysis with constant heating rates from 1 to 15 °C/min in air

Figure 9 shows the derivative of the mass change w.r.t. the temperature for the same experiments as in Figure 8. In all experiments, the rate of oxidation increases from 200 to about 500 °C then decreases except for a peak at around 600 °C. This momentary increase in the reaction rate can be related to another reaction pathway involving wüstite above 570 °C.

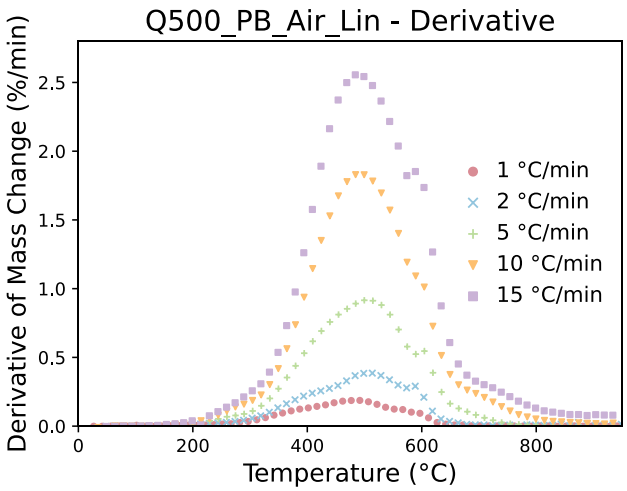

Figure 9. Derivative of the mass change with constant heating rates from 1 to 15 °C/min in air

The results of the TGA experiments with pure oxygen under linear temperature increases using the Q500 TGA apparatus are shown in Figure 10 and the corresponding derivatives in Figure 11. The curve profiles are very similar to the ones obtained with air. The rate of oxidation is slightly increased by the presence of pure oxygen. The sample of the experiment at 10 °C/min now also undergoes full oxidation. The wüstite peak seems even less important under these conditions and is even not visible for low heating rates. An explanation for this is that the oxidation in the presence of pure oxygen is more advance or even close to completion at 570 °C.

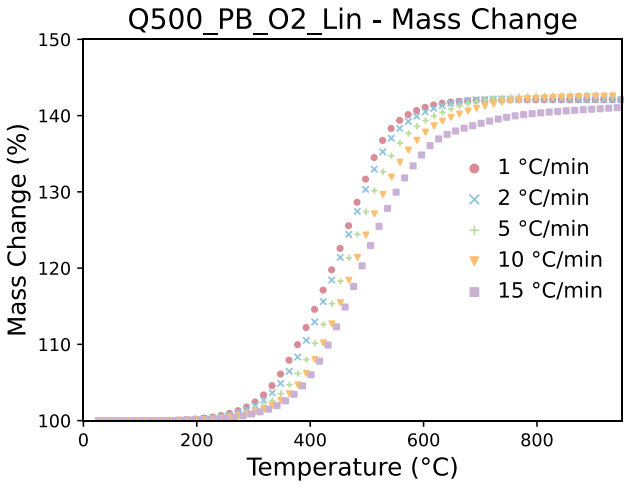

Figure 10. Thermogravimetric analysis with constant heating rates from 1 to 15 °C/min in oxygen

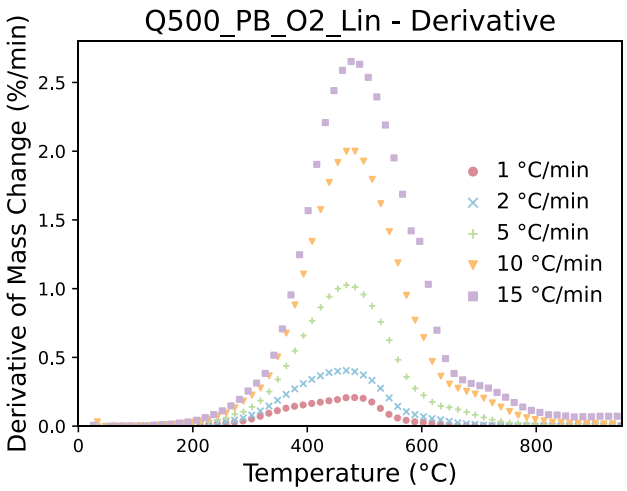

Figure 11. Derivative of the mass change with constant heating rates from 1 to 15 °C/min in oxygen

Further results under constant heating rates can be found in the supplementary materials. Figure S4 shows the with the second analyzer. The curves have a similar shape and the extent of oxidation is advanced at the end of the experiments, higher than 135% in all cases. But it appears more difficult to reach a complete oxidation with the second apparatus, which may find its origin in the difference in crucible shape and material. Variation of the powder is also given in Figure S4, but major differences can be detected. The influence of the mass variation at a temperature elevation of 5 °C/min can be seen in Figure S5. The curves almost overlap for the larger part of the experiments. A notable difference is that the final extent of oxidation is lower when higher masses are used.

4.4. Interpretation of the thermal analysis

4.4.1. Analysis from the TGA curves and characterization

The first conclusion that can be drawn from the TGA curves, both under isothermal condition as with an increase of the temperature, is that the rate of oxidation strongly increases with the temperature but also strongly decreases with the extent of oxidation. This is in agreement with a process limited by the diffusion of cations in the oxide layer. However, concerning the isothermal cases, it is quite obvious that under the present experimental configuration, the rate limiting process of the first stage is controlled by the external mass transfer of oxygen: the initial slopes are almost constant for various temperatures when the gas flow rate is kept constant and the slopes increase with both the gas flow rate and the concentration of oxygen. The second stage, on the other hand, seems to be limited by the oxide growth

mechanism internal to the particles, as the gas flow rate and oxygen concentration have no notable influence. This second controlling factor is highly temperature dependent, thus the transition occurs at higher extent of oxidation at higher temperatures. The fact that the transition from the first stage to the second can be explained as follow: As the temperature rises initially, the gas-controlled stage proceeds to a larger extent than if isothermal conditions could be maintained. Then, the cooling of the particles entrains a strong decrease of the rate of oxidation of the second growth controlling phenomenon, which becomes abruptly the limiting factor. A gradual increase of the temperature, that is stepwise, as in Figure X, or with a constant heating rate, avoid partly or totally the gas-transport limitations.

Figure X shows SEM images of powder A oxidized under various conditions. The first striking observation is the strong sintering of the particles. The external morphology of the samples oxidized at 400 °C is quite similar with the one at 5 °C/min up to an oxidation degree of about 50% (that means stopped at around 450 °C). Single original particles can still be identified but they are all glued to neighbor particles. This might explain the very strong deceleration of the oxidation with the extent of oxidation: the migration path of the charged species not only increases together with the oxide layer growth of single particles but also due to the trapping of particles among others. The associated decrease of the surface area might also be a reason for the reduction of the oxidation rate. Ultimately, the external surface becomes continuous, as evidenced by the SEM images of the sample oxidized under a constant temperature increase of 5 °C/min up to a temperature of 700 °C. This layer might prevent the oxidation of some of the iron particles in the center of the sample. Thus, a condition for a complete oxidation could be that the layer of particles on the crucible is very thin. It should be noted that the SEM images were performed on samples from experiments with an important initial sample weight to enable accurate XRD results. The SEM images suggest the presence of several layers (see here the broken particle in Figure X.d.). There is an external honeycomb-like layer, rather thin, around columnar grains, themselves surrounding other internal structures. Further SEM images under various magnification for powders A and B are given the supplementary materials. For the highest temperature cases, interpretation is made difficult from radical changes in the external surface morphologies, which may be due to restructuration of the oxides or from interaction between the sample and the crucible.

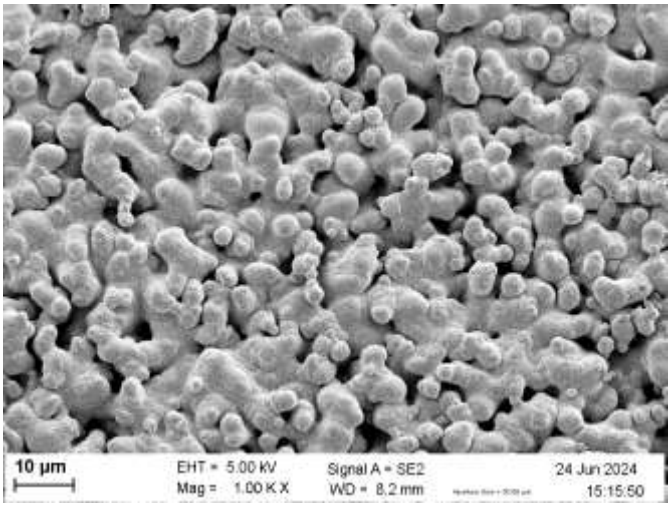

a.

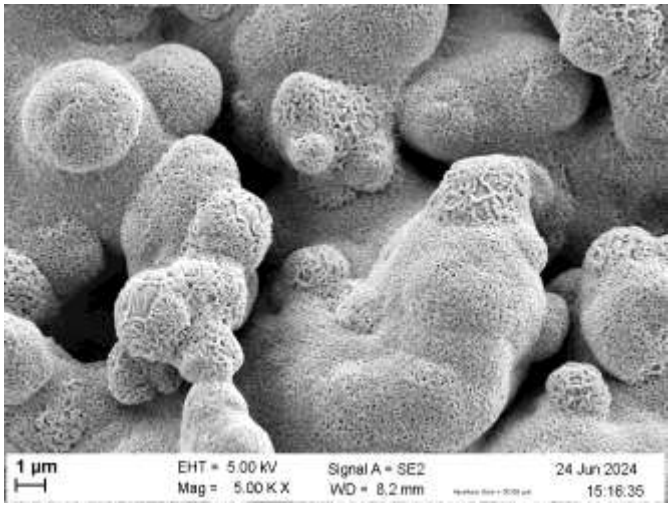

b.

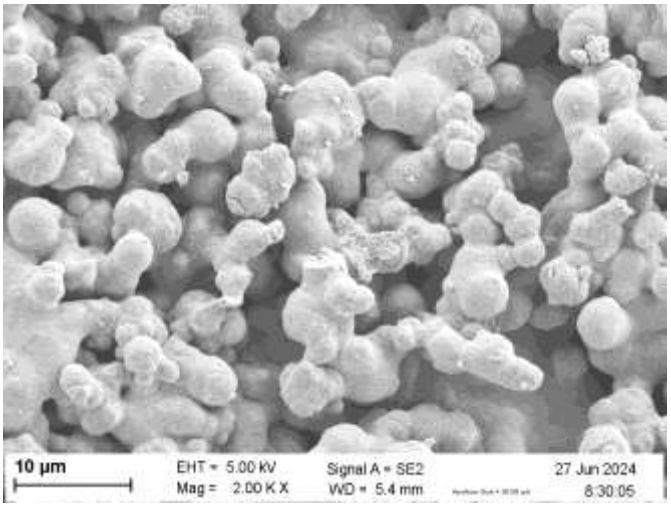

c.

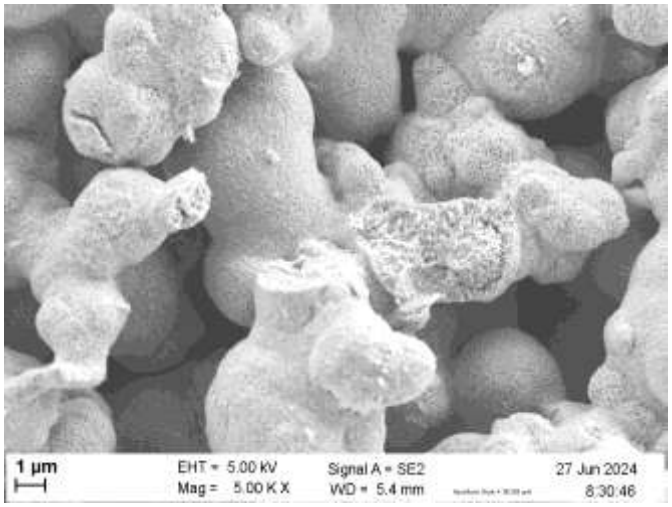

d.

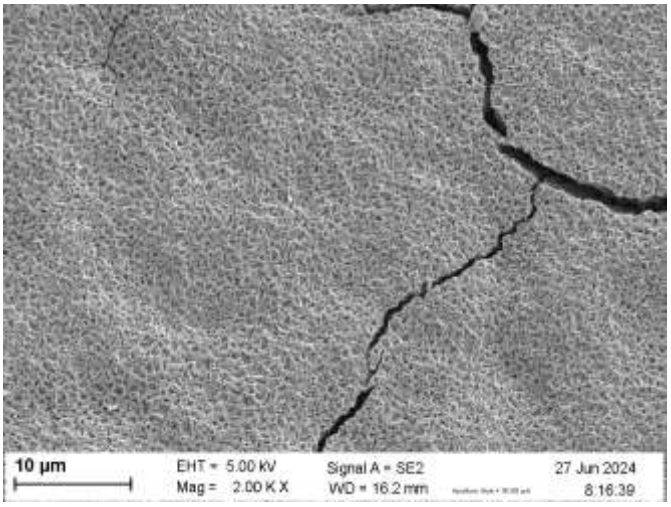

e.

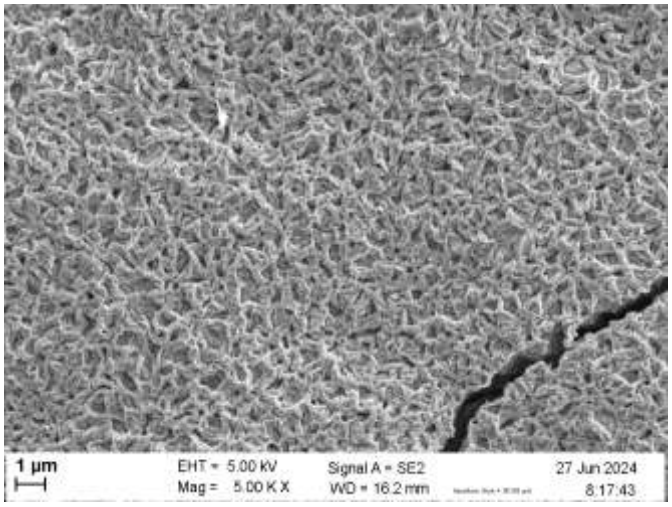

f.

Figure 12. SEM images of the powder A oxidized at 400 °C during one hour (a. and b.), oxidized under a constant temperature increase of 5 °C/min up to an oxidation extent of 50% (c. and d.), and oxidized under a constant temperature increase of 5 °C/min up to a temperature of 700 °C (e. and f.)

The XRD results presented in Figure X helps identifying the species of the previous SEM images. The diffraction patterns are presented in Figure X.a. and the corresponding phase composition in Figure X.b. The phase compositions are equivalent to extents of oxidation of 66, 55, and 77% for the cases isothermal at 400 °C, 5 °C/min up to an oxidation extent of around 50%, and 5 °C/min up to a temperature of 700 °C, respectively. The similarity between the SEM images of the first two cases is retrieved in the XRD results, with samples primarily composed of magnetite, but with an important amount of iron remaining, between 30 to 40%. In both cases, hematite is present but in amounts not exceeding 4%. The ratio of hematite to magnetite (around 5:95 at 400 °C) is therefore comparable to the analogous oxidation on iron strips. Only in the sample oxidized up to 700 °C wüstite could be detected, and this oxide presenting non-uniform stoichiometry. This latter sample also shows a larger hematite content and remaining iron. As low-weight samples should be fully oxidized at 700 °C, we can attribute the remaining iron in this high-weight sample to be the consequence of the impermeable layer previously discussed. XRD results from powder B is given in the supplementary materials, in which similar conclusions can be drawn.

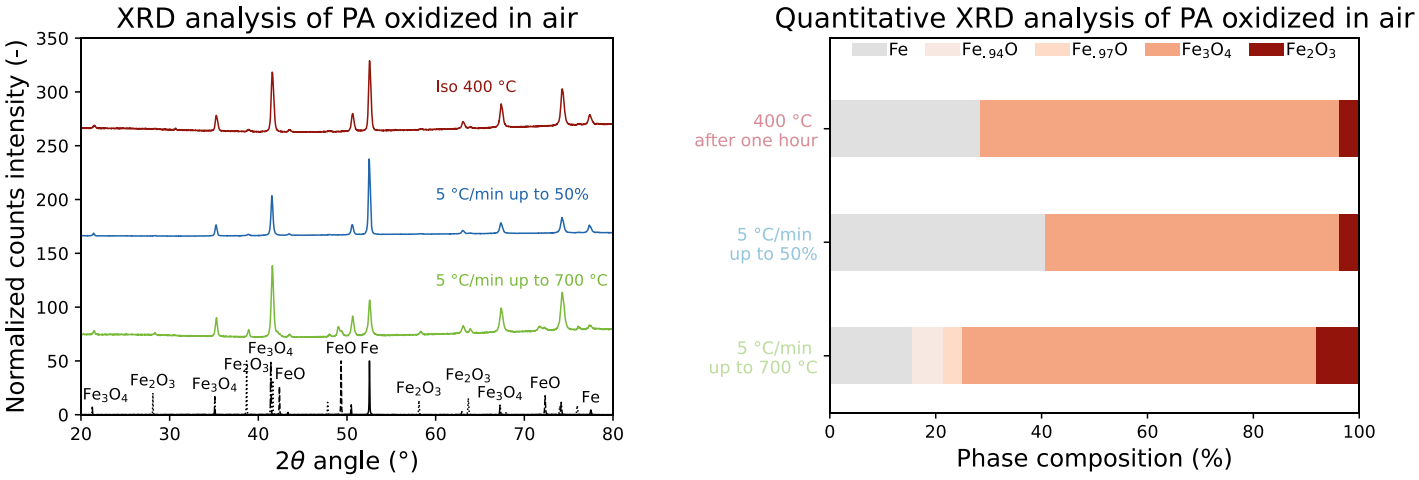

a. b.

Figure 13. XRD analysis of powder A oxidized in air

4.4.2. Proposed growth mechanism of single particles

On the basis of the SEM images of broken particles and the XRD data, we propose the mechanism illustrated in Figure X for the oxidation of single iron particles under 570 °C, which bares many similarity to the one of Bertrand et al. [25] on pure iron sheets oxidized at low temperatures (260–400 °C). The oxidation is primarily controlled by the outward growth of magnetite. Ferrous ions Fe^{2+}, ferric ions Fe^{3+},

and electrons migrate to the magnetite/hematite interface and hematite/air interface. Hematite grows according to the reaction:

$$2\ Fe^{3+} + 6\ e^{-} + 3/2\ O_2 \rightarrow Fe_2O_3. \qquad (X)$$

But hematite is also consumed by the reaction responsible for the outward growth of magnetite:

$$Fe^{2+} + 2\ e^{-} + 4\ Fe_2O_3 \rightarrow Fe_3O_4. \qquad (X)$$

If the process was only controlled by outward growths, porous cores should form. In the SEM image of the broken particle, no porous zones are visible. Thus, the oxidation process is completed by ionization of oxygen and inward short-circuit transport to the iron/magnetite interface:

$$2\ Fe^{3+} + Fe^{2+} + 4\ O^{2-} \rightarrow Fe_3O_4. \qquad (X)$$

The SEM image in Figure X indicate a duplex magnetite layer, similar to the description of Atkinson et al. [9], with an outer layer having a columnar structure and an inner layer more equi-axed.

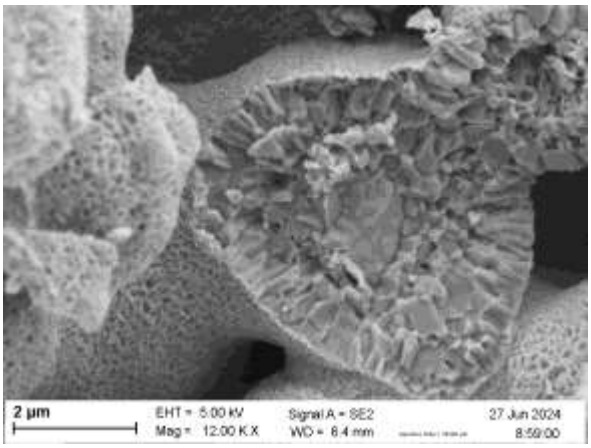

a.

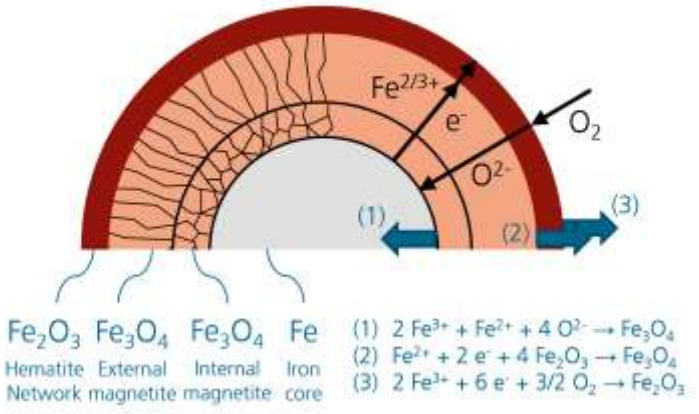

b.

Figure 14. XRD analysis of powder A oxidized in air

Following the proposed mechanism, all three growth rates are interdependent (the hematite growth depends on the total migration path, the magnetite outward growth depends on the availability of hematite, while the inward growth cannot proceed prior to the outward growth). This is evidenced by the uniformity of the layers around any particle and among multiple particles.

4.4.3. Kinetics of the oxidation process

Figure X. shows the results of the Kissinger–Akahira–Sunose method; a method used to derive the activation energy from TGA experiments with a constant heating rate. For more information on this method, the reader is referred to Vyazovkin et al. [47]. The symbol \beta that appears in the figure corresponds to the heating rate of the individual experiment. It was performed with the experiment in air and pure oxygen and at three conversion degrees, 0.25, 0.5, and 0.75. The values found are high, in the range 180-320 kJ/mol. A value of 220 kJ/mol is used in the following.

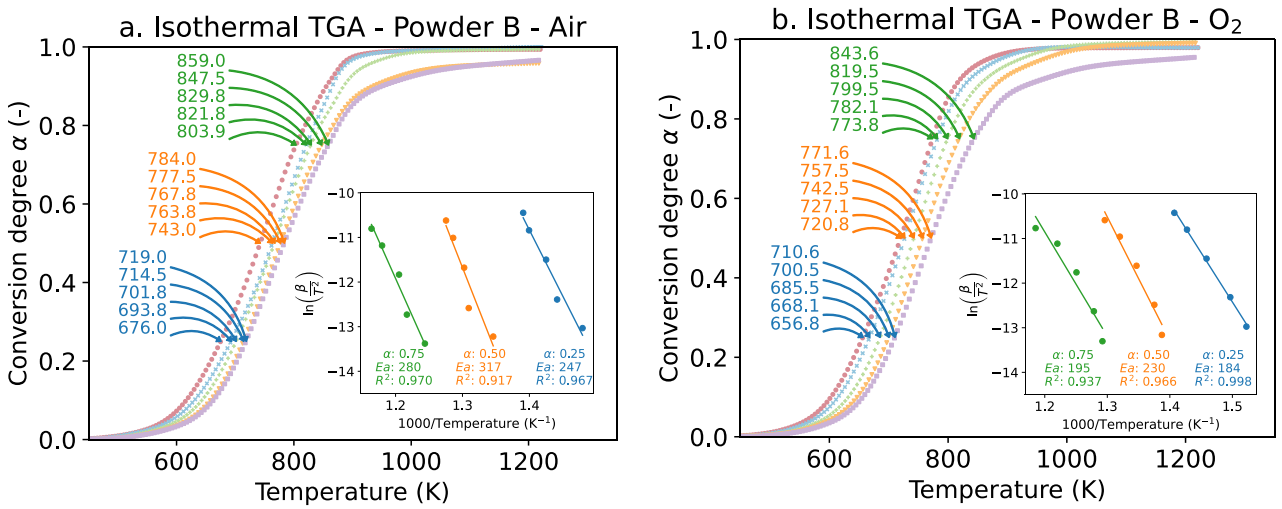

Figure 15. Kissinger–Akahira–Sunose method applied to the TGA tests with linear heating rates.

A decelerating profile could be associated with a phase-boundary, a diffusion, or a first order model, Furthermore, the truncated Sestak and Berggren model is investigated [47]. It assumes a reaction model in the general form:

$$f(\alpha) = \alpha^m(1-\alpha)^n, \qquad \text{(X)}$$

where m and n are parameters to determine. The effect of the atmosphere was accounted through:

$$\frac{\mathrm{d}\alpha}{\mathrm{d}t} = f(\alpha)k(T)\left(P_{O_2}/P_{tot}\right)^p. \qquad \text{(X)}$$

These parameters were determined from the experiments with linear temperature increase via the least-square method. The final values read n=2.3, m=-3, p=\ 0.5. Figure 8 shows both the modeling results using equation (12) and the experiments. The approach gives overall good agreement.

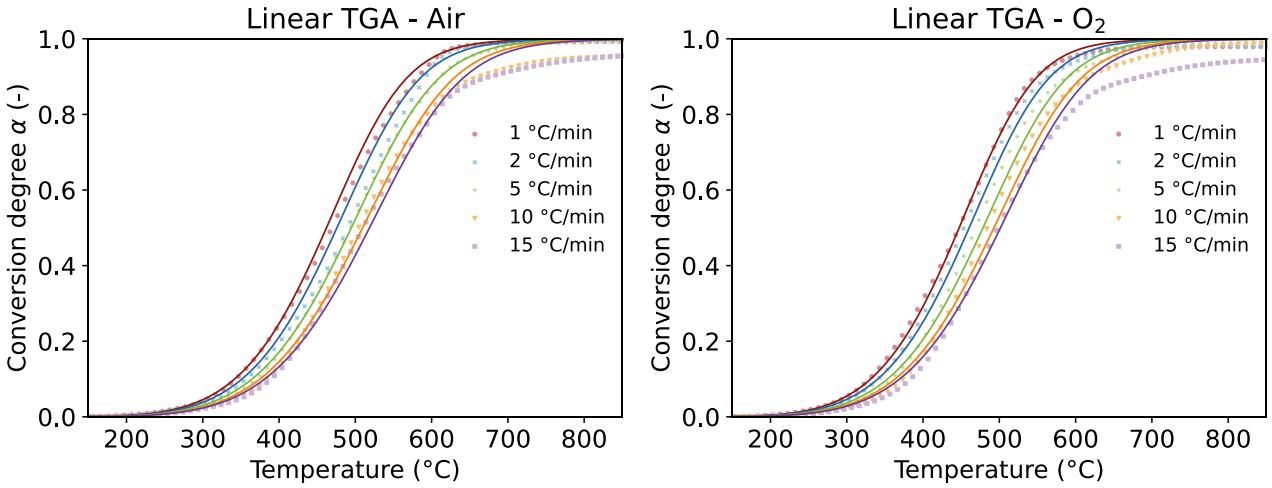

Figure 16. Comparison between the truncated Sestak and Berggren model and experiments for the thermogravimetric analysis with heating linear rates from 1 to 15 °C.

The same approach was tested on isothermal experiments using powder A and B and the same parameters: E_a,n, m, and p. The results are reported in Figure 8. To account for the initial external gas transfer limitation, the maximum between the initial slope (0.015 s-1) and the value given by Equation (12) was taken. It can be seen that good agreements can be obtained in the case of isothermal experiments with the parameters derived previously from dynamic experiments and for two different powders. The dependency on the temperature is especially well retrieved with powder A, suggesting a realistic value for the activation energy. For powder B, a good agreement is before all obtained at low temperatures, 300 and 350 °C. The underestimation in the initial stage could be due to the heat generated by the reaction, which is not reproduced in the model under isothermal conditions.

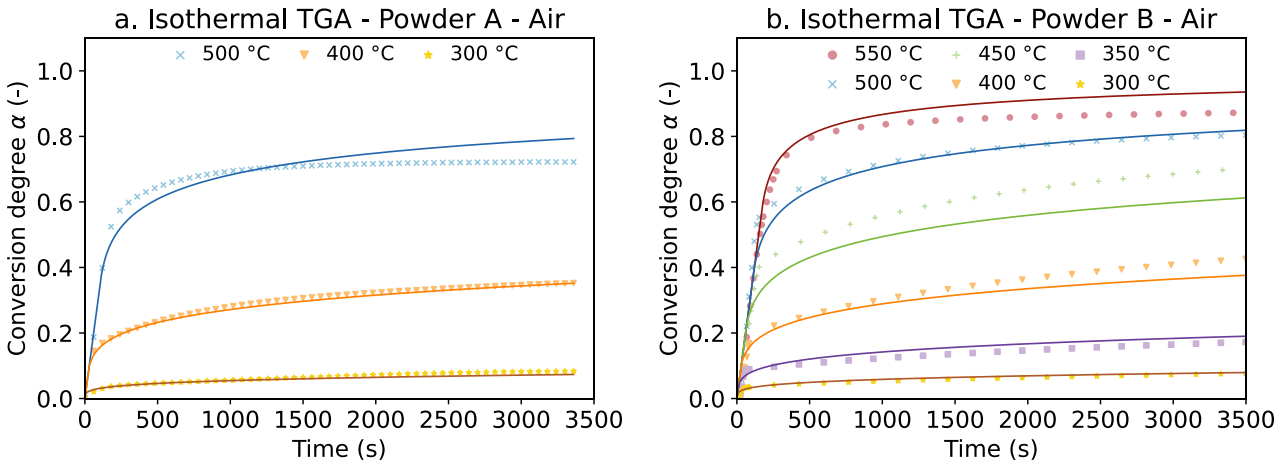

Figure 17. Comparison between the truncated Sestak and Berggren model and experiments for the isothermal thermogravimetric analysis.

5. Conclusions

Acknowledgements

This work was performed within the DLR project IronCircle® and the cluster project Clean Circles.

References

[1] J. M. Bergthorson, "Recyclable metal fuels for clean and compact zero-carbon power," *Progress in Energy and Combustion Science,* vol. 68, p. 169–196, 2018.

[2] J. M. Bergthorson, S. Goroshin, M. J. Soo, P. Julien, J. Palecka, D. L. Frost and D. J. Jarvis, "Direct combustion of recyclable metal fuels for zero-carbon heat and power," *Applied Energy,* vol. 160, p. 368–382, 2015.

[3] "Clean Circles," 2021. [Online]. Available: www.clean-circles.de. [Accessed 29 9 2021].

[4] *Iron Fuel Technology*.

[5] X. Mi, A. Fujinawa and J. M. Bergthorson, "A quantitative analysis of the ignition characteristics of fine iron particles," *Combustion and Flame,* vol. 240, p. 112011, 2022.

[6] J. Mich, D. Braig, T. Gustmann, C. Hasse and A. Scholtissek, "A comparison of mechanistic models for the combustion of iron microparticles and their application to polydisperse iron-air suspensions," *Combustion and Flame,* vol. 256, p. 112949, 2023.

[7] I. A. Bruce, "The oxidation behaviour of sintered iron," University of Aston, 1991.

[8] K. R. Lawless, "The oxidation of metals," *Reports on Progress in Physics,* vol. 37, no. 2, p. 231–316, 1974.

[9] A. Atkinson, "Transport processes during the growth of oxide films at elevated temperature," *Reviews of Modern Physics,* vol. 57, no. 2, p. 437–470, 1985.

[10] N. F. Mott, "The theory of crystal rectifiers," *Proceedings of the Royal Society of London. Series A. Mathematical and Physical Sciences,* vol. 171, no. 944, p. 27–38, 1939.

[11] N. Cabrera and N. F. Mott, "Theory of the oxidation of metals," *Reports on Progress in Physics,* vol. 12, no. 1, p. 163–184, 1949.

[12] C. Wagner, "Beitrag zur Theorie des Anlaufvorgangs," *Zeitschrift für Physikalische Chemie,* vol. 21B, no. 1, p. 25–41, 1933.

[13] C. Wagner, "Beitrag zur Theorie des Anlaufvorganges. II," *Zeitschrift für Physikalische Chemie*, vol. 32B, no. 1, p. 447–462, 1936.

[14] A. Atkinson, "Wagner theory and short circuit diffusion," *Materials Science and Technology*, vol. 4, no. 12, p. 1046–1051, 1988.

[15] M. H. Davies, M. T. Simnad and C. E. Birchenall, "On the Mechanism and Kinetics of the Scaling of Iron," *JOM*, vol. 3, no. 10, p. 889–896, 1951.

[16] D. Caplan, R. J. Hussey, G. I. Sproule and M. J. Graham, "The effect of FeO grain size and cavities on the oxidation of Fe," *Corrosion Science*, vol. 21, no. 9-10, p. 689–711, 1981.

[17] G. Garnaud and R. A. Rapp, "Thickness of the oxide layers formed during the oxidation of iron," *Oxidation of Metals*, vol. 11, no. 4, p. 193–198, 1977.

[18] J. Païdassi, "Sur la cinetique de l'oxydation du fer dans l'air dans l'intervalle 700–1250°C," *Acta Metallurgica*, vol. 6, no. 3, p. 184–194, 1958.

[19] G. W. Simmons, E. Kellerman and H. Leidheiser, "The Oxidation of Iron as Studied by Conversion Electron Mössbauer Spectroscopy," *Corrosion*, vol. 29, no. 6, pp. 227-223, 1973.

[20] D. Caplan and M. Cohen, "Scaling of iron at 500°C," *Corrosion Science*, vol. 3, no. 3, pp. 139-IN2, 1963.

[21] R. J. Hussey, G. I. Sproule, D. Caplan and M. J. Graham, "The growth and structure of oxide films formed on Fe in O2 and CO2 at 550C," *Oxidation of Metals*, vol. 11, no. 2, p. 65–79, 1977.

[22] D. Caplan and M. Cohen, "Effect of cold work on the oxidation of iron from 400–650 °C," *Corrosion Science*, vol. 6, no. 7, p. 321–335, 1966.

[23] D. Caplan, G. I. Sproule and R. J. Hussey, "Comparison of the kinetics ofhigh-temperature oxidation of Fe as influenced by metal purity and cold work," *Corrosion Science*, vol. 10, no. 1, p. 9–17, 1970.

[24] R. J. Hussey and M. J. Graham, "Some observations on void formation in Fe3O4 layers on Fe," *Corrosion Science*, vol. 21, no. 3, p. 255–258, 1981.

[25] N. Bertrand, C. Desgranges, D. Poquillon, M. C. Lafont and D. Monceau, "Iron Oxidation at Low Temperature (260–500 °C) in Air and the Effect of Water Vapor," *Oxidation of Metals*, vol. 73, no. 1-2, p. 139–162, 2010.

[26] L. Himmel, R. F. Mehl and C. E. Birchenall, "Self-Diffusion of Iron in Iron Oxides and The Wagner Theory of Oxidation," *JOM*, vol. 5, no. 6, p. 827–843, 1953.

[27] W. E. Boggs, R. H. Kachik and G. E. Pellissier, "The Effect of Oxygen Pressure on the Oxidation of Zone-Refined Iron," *Journal of The Electrochemical Society*, vol. 112, no. 6, p. 539, 1965.

[28] Z. Szklarska-Smialowska and J. Jurek, "Ellipsometric Studies on Iron Oxide Film Growth at 100 to 350 C," *Corrosion*, vol. 32, no. 7, p. 294–297, 1976.

[29] H. Sakai, T. Tsuji and K. Naito, "Oxidation of Iron in Air between 523 and 673 K," *Journal of Nuclear Science and Technology*, vol. 22, no. 2, p. 158–161, 1985.

[30] M. J. Graham, S. I. Ali and M. Cohen, "Low Temperature Oxidation (24° to 200°C) and Krypton Adsorption Studies on Polycrystalline and Single Crystal Iron Surfaces," *Journal of The Electrochemical Society*, vol. 117, no. 4, p. 513, 1970.

[31] D. A. Channing and M. J. Graham, "A study of iron oxidation processes by Mössbauer spectroscopy," *Corrosion Science*, vol. 12, no. 3, p. 271–289, 1972.

[32] K. Reddy and A. R. Cooper, "Oxygen Diffusion in MgO and α-Fe 2 O 3," *Journal of the American Ceramic Society*, vol. 66, no. 9, p. 664–666, 1983.

[33] R. Takagi, "Growth of Oxide Whiskers On Metals at High Temperature," *Journal of the Physical Society of Japan*, vol. 12, no. 11, p. 1212–1218, 1957.

[34] I. Svedung, B. Hammar and N.-G. Vannerberg, "The effect of recrystallization on the oxide scale composition and growth of whiskers during the oxidation of pure iron," *Oxidation of Metals*, vol. 6, no. 1, p. 21–44, 1973.

[35] D. A. Voss, E. P. Butler and T. E. Mitchell, "The Growth of Hematite Blades during the High Temperature Oxidation of Iron," *Metallurgical Transactions A*, vol. 13, no. 5, p. 929–935, 1982.

[36] L. Yuan, Y. Wang, R. Cai, Q. Jiang, J. Wang, B. Li, A. Sharma and G. Zhou, "The origin of hematite nanowire growth during the thermal oxidation of iron," *Materials Science and Engineering: B,* vol. 177, no. 3, p. 327–336, 2012.

[37] O. Lupan, V. Postica, N. Wolff, O. Polonskyi, V. Duppel, V. Kaidas, E. Lazari, N. Ababii, F. Faupel, L. Kienle and R. Adelung, "Localized Synthesis of Iron Oxide Nanowires and Fabrication of High Performance Nanosensors Based on a Single Fe2 O3 Nanowire," *Small,* vol. 13, no. 16, p. 1602868, 2017.

[38] E. N. Lysenko, A. P. Surzhikov, S. P. Zhuravkov, V. A. Vlasov, A. V. Pustovalov and N. A. Yavorovsky, "The oxidation kinetics study of ultrafine iron powders by thermogravimetric analysis," *Journal of Thermal Analysis and Calorimetry,* vol. 115, no. 2, p. 1447–1452, 2014.

[39] D. Wen, P. Song, K. Zhang and J. Qian, "Thermal oxidation of iron nanoparticles and its implication for chemical-looping combustion," *Journal of Chemical Technology & Biotechnology,* vol. 86, no. 3, p. 375–380, 2011.

[40] C. Mandilas, G. Karagiannakis, A. G. Konstandopoulos, C. Beatrice, M. Lazzaro, G. Di Blasio, S. Molina, J. V. Pastor and A. Gil, "Study of Oxidation and Combustion Characteristics of Iron Nanoparticles under Idealized and Enginelike Conditions," *Energy & Fuels,* vol. 30, no. 5, p. 4318–4330, 2016.

[41] E. N. Lysenko, A. P. Surzhikov, E. V. Nikolaev, V. A. Vlasov and S. P. Zhuravkov, "The oxidation kinetic study of mechanically milled ultrafine iron powders by thermogravimetric analysis," *Journal of Thermal Analysis and Calorimetry,* vol. 134, no. 1, p. 307–312, 2018.

[42] C. Kuhn, A. Knapp, M. P. Deutschmann, J. Spielmann, S. Tischer, U. I. Kramm, H. Nirschl and O. Deutschmann, "Iron as Recyclable Metal Fuel: Unraveling Oxidation Behavior and Cyclization Effects Through Thermogravimetric Analysis, Wide-Angle X-ray Scattering and Mössbauer Spectroscopy," *ChemSusChem,* vol. 17, no. 15, p. e202400351, 2024.

[43] M. Fedoryk, B. Stelzner, S. Harth and D. Trimis, "Laminar burning velocity measurements and stability map determination of Fe-N2/O2 mixtures in a tube burner," 2023.

[44] C. Sarkar and H. Hirani, "Effect of Particle Size on Shear Stress of Magnetorheological Fluids," *Smart Science,* vol. 3, no. 2, 2015.

[45] A. Soria-Verdugo, M. T. Morgano, H. Mätzing, E. Goos, H. Leibold, D. Merz, U. Riedel and D. Stapf, "Comparison of wood pyrolysis kinetic data derived from thermogravimetric experiments by model-fitting and model-free methods," *Energy Conversion and Management,* vol. 212, p. 112818, 2020.

[46] Q. Fradet, M. Kurnatowska and U. Riedel, "Thermochemical reduction of iron oxide powders with hydrogen: Review of selected thermal analysis studies," *Thermochimica Acta,* vol. 726, p. 179552, 2023.

[47] S. Vyazovkin, A. K. Burnham, J. M. Criado, L. A. Pérez-Maqueda, C. Popescu and N. Sbirrazzuoli, "ICTAC Kinetics Committee recommendations for performing kinetic computations on thermal analysis data," *Thermochimica Acta,* vol. 520, no. 1-2, p. 1–19, 2011.

[48] L. Choisez, K. Hemke, Ö. Özgün, C. Pistidda, H. Jeppesen, D. Raabe and Y. Ma, "Hydrogen-based direct reduction of combusted iron powder: Deep pre-oxidation, reduction kinetics and microstructural analysis," *Acta Materialia,* vol. 268, p. 119752, 2024.

[49] J. Païdassi, "Sur l'oxydation du protoxyde de fer dans l'air dans l'intervalle 600–1350°c," *Acta Metallurgica,* vol. 6, no. 3, p. 219–221, 1958.